Monitoring imbibition dynamics at tissue level in Norway spruce using X-ray imaging

Benoît Martin, Julien Colin, Pin Lu, Mahamadou Mounkaila, Joel Casalinho, Patrick Perré, Romain Rémond

HAL Id: hal-03487090
https://hal.science/hal-03487090

Original Article

Benoît Martin*, Julien Colin, Pin Lu, Mahamadou Mounkaila, Joel Casalinho, Patrick Perré
and Romain Rémond

Monitoring imbibition dynamics at tissue level in Norway spruce using X-ray imaging

Abstract: The study of moisture migration in Norway
Spruce may reduce the discrepancy between measure-
ments and simulations of transfers in buildings and thus
be helpful for improving their performance and durability.
For this purpose, X-ray imaging was used to study moisture
migration in Norway spruce during imbibition at tissue
level. Moisture content kinetics in earlywood and late-
wood, based on X-ray attenuation, was observed and
measured through rigorous protocol. The imbibition pro-
cess was studied in both longitudinal and radial directions.
The results showed an easier migration of liquid in late-
wood than in earlywood in the longitudinal uptake. In the
radial direction, the impact of compression wood as a
barrier and the role of the anatomical structure in the liquid
migration were highlighted by the direct visualization of
filled tracheids.

*Corresponding author: Benoît Martin, LERMAB, Université de
Lorraine, ENSTIB, 27, Rue Philippe Séguin, Epinal 88051, France; and
Université Paris-Saclay, CentraleSupélec, Laboratoire de Génie des
Procédés et Matériaux, SFR Condorcet FR CNRS 3417, Centre Européen
de Biotechnologie et de Bioéconomie (CEBB), Pomacle, France,
E-mail: b.martin@univ-lorraine.fr. https://orcid.org/0000-0001-
6816-4288
Julien Colin and Patrick Perré, Université Paris-Saclay,
CentraleSupélec, Laboratoire de Génie des Procédés et Matériaux,
SFR Condorcet FR CNRS 3417, Centre Européen de Biotechnologie et
de Bioéconomie (CEBB), Pomacle, France; and Université Paris-
Saclay, CentraleSupélec, Laboratoire de Génie des Procédés et
Matériaux, Gif-sur-Yvette, France
Pin Lu and Mahamadou Mounkaila, Université Paris-Saclay,
CentraleSupélec, Laboratoire de Génie des Procédés et Matériaux,
SFR Condorcet FR CNRS 3417, Centre Européen de Biotechnologie et
de Bioéconomie (CEBB), Pomacle, France
Joel Casalinho, Université Paris-Saclay, CentraleSupélec, Laboratoire
de Génie des Procédés et Matériaux, Gif-sur-Yvette, France
Romain Rémond, LERMAB, Université de Lorraine, ENSTIB, 27, Rue
Philippe Séguin, Epinal 88051, France

1 Introduction

As wood is a hygroscopic material, its moisture content
(MC) varies according to the surrounding air conditions
and may also change through contact with liquid water. In
a piece of wood, water can be present as liquid, vapor, or
bound to the lignocellulosic material. The fiber saturation
point (FSP) marks a change of water behavior in wood, at a
moisture content close to 30% dry basis depending on
temperature and species (Siau 1984). Below this point, the
change in moisture content causes dimensional variations
likely to induce internal stresses if the shrinkage field is not
geometrically compatible (McMillen 1958; Schmidt et al.
2019; Tiemann 1919). In building applications, the moisture
content of the engineering wood products must remain
close to their intended usage to ensure mechanical and
physical performance. In recent years, the growing number
of wooden skyscrapers and large wooden buildings has led
to an increase in the duration of construction, which can
take up to several months. During the construction phase,
structural elements may be exposed to outdoor weather
conditions, namely rain. Thus, a drying period is required
before adding insulation and exterior or interior coatings
(Lepage 2012). In addition, during the lifespan of a build-
ing, engineered wood products may be exposed to water
infiltration from the exterior envelope or water supply
system (Tietze et al. 2017). These localized increases in
moisture content within the envelope can create favorable
conditions for biological degradation when they remain
close to or above the FSP for several weeks (Johansson et al.
2013; Viitanen 1994). To address these issues, numerical
tools can estimate the necessary drying time or be used as a
design tool for composite walls. However, discrepancies
between measurements and simulations remain, limiting
the numerical design solutions (Johansson and Kifetew
2010; Krabbenhoft and Damkilde 2004). Thus, a better

understanding of water migration in wood is required to improve numerical models. Moisture uptake in a dried piece of wood involves coupled heat and mass transfers due to the phase change of water and its affinity for lignocellulosic material. To access the MC in a piece of wood and the amount of each state of water (liquid or bound), various methods can be used (Niemz and Mannes 2012; Perré 2011; Phillipson et al. 2007). One of the simplest and most commonly used methods to measure MC is the oven-dry—or gravimetric—method. However, this assesses only an average MC (NF EN 13183-1 2002). By cutting a sample into several layers and weighting them, MC distribution can be obtained, but this procedure is destructive and tedious (De Meijer and Militz 2000).

Moreover, the results may be affected by the cutting. Another way to estimate wood moisture content is to use the electrical resistivity between two inserted moisture pins. This electrical method is useful for *in-situ* measurements in wood structures below the FSP, taking into account the location of the sensors in relation to the wood grain orientation (NF EN 13183-2 2002; Tiitta and Olkkonen 2002). In a laboratory, the moisture distribution can be assessed using nuclear magnetic resonance (NMR), a non-invasive and non-destructive technique based on the relaxation time of hydrogen protium (^{1}H) after being exposed to a magnetic field (Hameury and Sterley 2006; Passarini et al. 2015). In addition, the state of water (bound or free) can be assessed according to relaxation time (Almeida et al. 2007; Gezici-Koç et al. 2017). Using magnetic field gradients, magnetic resonance imaging (MRI) allows access to a spatial distribution of water. Nevertheless, its anatomy remains unavailable because nuclei with zero nuclear spin, such as carbon-12 and oxygen-16, present in the lignocellulosic wall, cannot give off NMR signals (Houts et al. 2004; Zhou et al. 2018). Another technology, based on the attenuation of ionizing radiation—X-ray or neutron—, can be used to visualize moisture migration in a piece of wood. Numerous works have shown the great potential of this technique in observing water uptake in various materials (Baettig et al. 2006; Derome et al. 2005; Desmarais et al. 2016; Roels and Carmeliet 2006; Sandberg and Salin 2012). Considering the specific properties of wood (hygroscopicity, shrinkage, wettability, etc.), the accurate assessment of MC distribution over time remains the main challenge of dynamic moisture uptake measurement.

In this study, X-ray imaging was used to assess moisture migration in Norway spruce during imbibition in longitudinal and radial directions. The method used was based on 2D imaging to measure the evolution of the MC field over time. The following section will present the detailed sample preparation and image acquisition, followed by the image processing method, involving a rigorous X-ray beam attenuation treatment to distinguish water from lignocellulosic material. Next, the measurement protocol to obtain the spatial MC distribution according to migration direction will be described. Finally, the results will be analyzed, highlighting the role of the anatomical structure of wood in the moisture uptake process.

2 Materials and methods

2.1 Materials and sample preparation

The species studied was the Norway spruce (*Picea abies*), which is widely used in wooden constructions (Ramage et al. 2017). The samples were extracted from a board located at the base of a tree trunk with visible pith and cambium, collected in the Auvergne region of France. A total of 73 annuals rings were counted, with an average thickness of 2 mm. A precision cutting machine (SECOTOM 50, Struers) was used to process the samples according to the main growth directions of wood and to obtain the dimensions indicated in Table 1.

The samples were rectangular to facilitate observation of the water uptake along the longitudinal and radial directions using 2D X-ray imaging. The annual ring borders were clearly visible, making it possible to identify latewood (dark) and earlywood (light) zones within the annual rings. Rigorous sample preparation was established to control the moisture content at all stages. First, the sample was cut and divided into two parts, making sure they had the same annual rings. One part was used for the imbibition experiment, and the other was used to measure the initial moisture content with the oven-drying method. The two specimens were stored in a climatic chamber set at 25 °C and 50% relative humidity until constant masses were reached.

To impose one-dimensional moisture flow in the wood during imbibition, the surfaces parallel to the water uptake were covered with a regular layer of waterproof sealant (Rubson, Liquid rubber plus). The two other surfaces were uncovered (additional information in Appendix), and the coated surfaces had been previously sanded with P360 sandpaper. After this, two coated layers were applied, and the final length of the sample was then cut using a microtome (Thermo Scientific, Sliding Microtome HM 450). Before and after each stage of sample preparation, the size and weight of the sample were measured.

Table 1: Dimensions of samples and locations in the plank.

Reference	Dimensions (mm)			Number of growth ring (from pith)
	Length [a]	Width [b]	Thickness [b]	
Sample A	30.80 (L)	8.70 (R)	3.07 (T)	42–46
Sample B	29.91 (R)	8.90 (T)	2.09 (L)	38–52

[a]Direction of water uptake direction: longitudinal (L), radial (R).
[b]Direction perpendicular to water uptake direction: longitudinal (L), radial (R), tangential (T).

2.2 X-ray imaging

2.2.1 Experimental setup: A custom device was entirely designed and conceived to be implemented in the nano-tomograph (RX Solutions, EasyTom XL Ultra 150-160). Particular caution was taken to maintain a constant liquid water level during the experiment using a closed-loop system composed of two containers, a water pump, and an overflow (Figure 1-Detail A). When the pump was switched on, it delivered the distilled water to the upper container, allowing imbibition to be started or stopped at the desired time. An aluminum sample holder was designed to maintain the sample above the water surface, leaving the upper and lower faces open to mass transfer. The sample is positioned on the holder using a small 3D printed piece. This holder was fixed on a Newport linear translation axis to adjust the level of free water. In addition, the environmental conditions during the tests (temperature and relative humidity) were monitored using an SHT85 capacitive sensor (Sensirion AG). The water system supply and sample holder were positioned inside a tomograph for image acquisition. A 3D reconstruction requires several dozen minutes, incompatible with the study of short-term phenomena. Thus, the protocol was based on 2D images (or radiography), allowing one image every 10 s, suitable to follow the fast liquid migration through the material during imbibition. As they provided the best trade-off between acquisition time and spatial resolution, the sealed micro-focus X-ray source (20 μm of focus size under the present operating conditions) and the CCD detector (9 μm of pixel size) available on the equipment were used. In 2D imaging, spatial resolution is a function of the distances between the observed object, the X-ray source, and the detector.

Additionally, the thickness of the observed object plays a role in the sharpness of the image regarding the large beam angle. It is important to take this effect into account to define the annual rings of wood clearly. To minimize this beam angle effect, the source-detector distance was maximized (ca. 1 m), and the sample was positioned as closely as possible to the detector (Figure 1). The small pixel size of the detector, together with the small sample thickness and the small X-ray beam angle, allowed the lumens filled by water to be clearly observed during radial direction imbibition. In this direction, the lumens were aligned with the X-ray beam. The operating conditions of the experimental setup were saved in the software controlling the

tomograph to repeat precisely the same image sequence at chosen lapse times, both during sample preparation and the imbibition test.

2.2.2 Image acquisition: The operating conditions of the X-ray source and the CCD detector were chosen to fulfill the requirements of the wooden material and the velocity of water uptake, namely at short times. The following parameters were chosen as best compromise for image acquisition:

- The X-ray source voltage was set at 90 kV and intensity at 200 μA with a focal spot size of 20 μm,
- The CCD detector was set at 16 bits with a binning of 2×2 to obtain 1344×2016 pixels, 18×18 μm^2 each (24.2×36.3 mm^2).
- Exposure time was set to 10 s per image.

The experiments lasted four days. The images were grabbed continuously for 6 h to follow the rapid water uptake at the beginning of the imbibition.

2.2.3 Image processing: The image processing step must be rigorous to obtain accurate moisture content in the sample using the X-rays transmission field (Perré and Thiercelin 2004). The steps are as follows: noise reduction, spatial correction of X-ray beam heterogeneity, and temporal correction of the source/detector variations.

The noise due to cosmic particles was reduced by a median filter over 10 successive images I for each pixel (i, j). Next, the incident X-ray flux is not uniform over the surface of the sample because the X-ray beam was divergent with a radiation intensity depending on the incidence angle. Thus, a spatial correction was applied by introducing the transmission $T(t)$ according to Equation (1):

$$T(t,i,j) = \frac{I(t,i,j) - I_B(t_0,i,j)}{I_0(t_0,i,j) - I_B(t_0,i,j)} \tag{1}$$

with $I_0(t_0)$ the reference image without sample taken with the same operating conditions and $I_B(t_0)$ the black field image corresponding to the offset of the grey level of the CCD detector grabbed without X-ray emission.

Finally, the time variation of the source/detector chain was corrected by using one part of the image $T(t)$ apart from the sample—the region of interest $ROI_{correct}$—and compared its average transmission
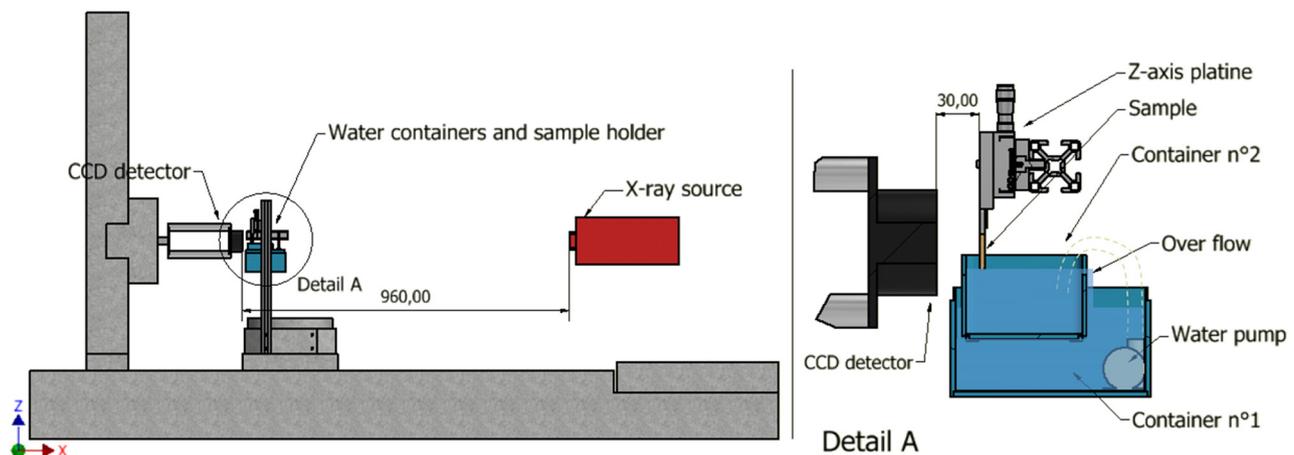

Figure 1: Scheme of the experimental setup of 2D X-ray imaging.

value $\langle T(t)\rangle[\text{ROI}_{\text{correct}}]$ to that of the same part of image $T(t_0)$ according to Equation (2):

$$T_{\text{correct}}(t,i,j) = \frac{T(t,i,j) < T(t_0) > [\text{ROI}_{\text{correct}}]}{<T(t)>[\text{ROI}_{\text{correct}}]} \qquad (2)$$

$\langle T_0\rangle[\text{ROI}_{\text{correct}}]$ being calculated from the reference image T_0 according to Equation (1), it equals to 1.

An example of this image processing is illustrated in Figure 2, with the grey level distribution of the image before (Figure 2a) and after noise reduction converted in 16 bits (Figure 2b). In the corrected image (Figure 2b), the peak located close to the grey value equal to 2000 was due to the aluminum sample holder with high X-ray attenuation. The peak with the grey values between 8000 and 9000 corresponded to the incident X-ray beam called background. The grey value distribution of the spruce sample at the equilibrium moisture content at 9.87% consisted of a peak corresponding to the earlywood (around 7000), followed by a shoulder corresponding to the latewood (darker grey than earlywood due to higher attenuation).
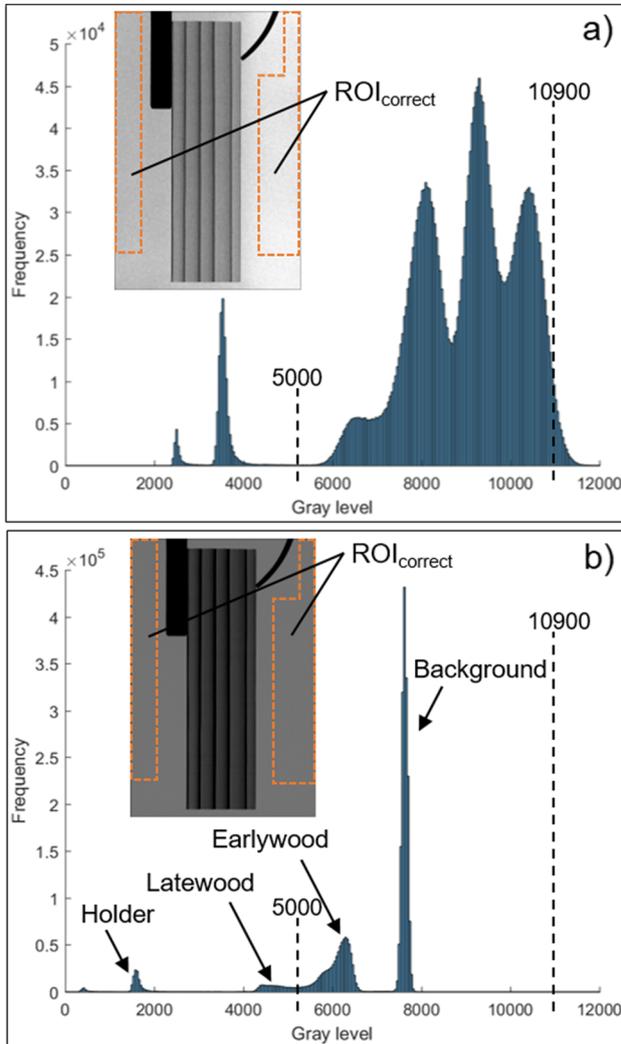

Figure 2: Distribution of grey level before (a) and after (b) image processing. Vertical dashed lines represent the limit of brightness and contrast of the inset image.

2.3 Moisture content determination

2.3.1 X-ray transmittance as a function of moisture content: The measurement of MC in wood or other porous materials using X-ray imaging is based on water X-ray attenuation (Cullity 1956; Guinier 1964). The Beer–Lambert law describes the intensity of the transmitted beam I when a monochromatic beam of energy (E) passes through a material of chemical composition (C), density (ρ), and thickness along the X-ray beam (d):

$$I(E) = I_0(E) \cdot \exp(-\mu(E,C) \cdot \rho \cdot d) \qquad (3)$$

with I_0 the intensity of the incident beam and μ the mass attenuation coefficient.

In the case of wet material, the respective densities of lignocellulosic material and water can be considered to constitute a two-phase component. The Beer–Lambert law can then be written as follows to calculate the attenuation for a monochromatic X-ray beam:

$$T(E) = \frac{I(E)}{I_0(E)} = \exp(-(\mu_0(E) \cdot \rho_0 + \mu_l(E) \cdot \rho_l) \cdot d) \qquad (4)$$

with T as the transmittance at a specific energy E, μ_0 the mass attenuation coefficient of anhydrous wood in m^2/kg, μ_l the water mass attenuation coefficient in m^2/kg, ρ_0 the density of anhydrous wood in kg/m^3, ρ_l the water density in kg/m^3, and d the sample thickness in m.

From Equation (4), an equivalent density can be obtained from a weighted average of dry wood and water densities. For a monochromatic beam, the logarithm of transmittance therefore linearly depends on this equivalent density. However, in the case of a polychromatic X-ray beam, Equation (4) should be integrated over the entire energy spectrum. As the attenuation depends on energy, the spectrum changes along its path (beam hardening); in this case, the simple additive relationship between the logarithm of transmittance, wood density, and water density vanished. A calibration step is thus required to obtain the attenuation function shape and the weighting factors specific to the X-ray chain acquisition at the operating conditions. This could be done properly using a spectrometric detector (Perré and Thiercelin 2004). However, in the case of the 2-D detector used in this study, the spectral distribution of the polychromatic X-ray beam as well as the polychromatic behavior of the detector are unknown; instead, only the integral values (I and I_0) measured by the detector on each pixel of the projection images were known (Pease et al. 2012). To this end, a simple non-linear relation (Equation (5)), taken from Bouali et al. (2012), was used to link the transmittance T to the equivalent surface density ρ_{eq}^* (kg/m^2):

$$\ln(T) = L_0 \cdot \rho_{\text{eq}}^* + L_1 \cdot \left(1 - \exp(-\rho_{\text{eq}}^*/\lambda)\right) \qquad (5)$$

where L_0 defines the initial slope of the curve (attenuation before any beam hardening), and L_1 and λ are the coefficients linked to the progressive hardening of the polychromatic energy effect. Therefore, L_1 is the slope obtained for the highest energy contained and detected in the polychromatic beam. All coefficients are specific to the source-detector chain at the operating conditions.

Furthermore, ρ_{eq}^* takes into account the two phases of the wet material (wood and water) as well as the sealant in the same expression:

$$\rho_{\text{eq}}^* = \frac{\rho_0^* \cdot (X + \alpha) + \rho_{\text{sealant, apparent}}^*}{\epsilon} \qquad (6)$$

with ρ_{eq}^* the equivalent surface density (kg/m²), ρ_0^* the surface density of wood (kg/m²), X the moisture content (–), α the weighting factor for the attenuation of dry wood with respect to the attenuation of water (–), $\rho_{sealant,\,apparent}^*$ the apparent surface density of the sealant (kg/m²), and ϵ the surface swelling (–).

The surface density ρ^* (kg/m²) can be expressed as follows:

$$\rho^* = \rho \cdot d \qquad (7)$$

with ρ the density (kg/m³) and d the length of the sample crossed by the X-ray beam (m).

A swelling correction is needed because the swelling of wood reduces the surface density. Thus, the surface swelling ϵ (Equation (8)) is determined by calculating the surface change of each ROI n from the initial stage (details of the positions of the ROIs in both imbibition directions are shown in Figure 4).

$$\epsilon(t) = \frac{S_{ROI_n}(t)}{S_{ROI_n}(t_0)} \qquad (8)$$

The attenuation ratio between lignocellulosic material and attenuation is taken into account through the factor α. It can be considered as constant beyond 80 keV according to the database XCOM from the National Institute of Standard and Technology (NIST) (Seltzer 1987), in spite of the hardening of the polychromatic X-ray beam (Pease et al. 2012).

The values of parameters L_0, L_1, λ, and α were identified by a calibration step, using parallelepipedal samples of *Sorbus torminalis* of various thicknesses (from 0.86 to 8.89 mm) without sealant. This species was chosen because of its homogeneous anatomical structure, which provides a regular density along the annual ring. This property allowed consideration of a similar surface density for all samples. A series of projections for each thickness were performed under two different states: air-dried (MC ≃ 8%, d.b.) and fully saturated in water (MC ≃ 125%, d.b.). The reference MC was determined using the gravimetric method before and after each acquisition. The values of the coefficients L_0, L_1, λ, and α were identified simultaneously using the GRG non-linear solver (Excel), minimizing the gap between numerical and experimental data (least-squares method). The results are depicted in Figure 3, with the corresponding values of the coefficients in Table 2.

From the other parameters of the model (L_0, L_1, and λ), α depends on species. After calibration, its value can be adjusted from one species to another using a single X-ray measurement at a known moisture content. In this study, one last step of the calibration protocol was required to identify the spatial distribution of $\rho_0^\star$ and $\rho_{sealant,\,apparent}^\star$ in Equation (6). For this purpose, the acquisition of the image according to the protocol detailed in 2.2.2 and 2.2.3 was performed before and after coating on the sample (respectively $T_{uncoated}$ and T_{coated}). Finally, the MC of the sample was carefully held constant during these steps.

2.3.2 Spatial discretization: The evolution of the moisture distribution in the sample was evaluated over regions of interest (ROI) using a custom MATLAB script. For the imbibition experiments in the longitudinal direction, the height of the sample was discretized into 59 adjacent ROIs of 0.52 mm height (Figure 4a). For the imbibition experiments in the radial direction, the height of the sample was discretized according to the growth rings. For each ROI of the sample, the ROI used for time-correction (ROI$_{correct}$ of Equation (2)) was chosen beside the sample at the same height. This precaution was
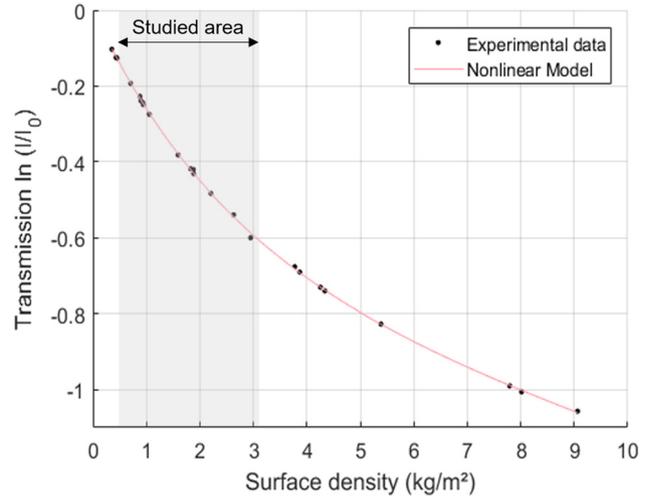

Figure 3: Experimental data from Sorbus samples of different thicknesses and moisture contents with the non-linear fitting curve (Equation (5)). The range of surface densities used later in this work is represented in grey.

adopted to compensate for a slightly non-uniform X-ray absorption along the height of the corrected image due to the evaporation of water from the water tank.

To highlight the density contrast and its effect on imbibition kinetic, ROIs were defined in earlywood and latewood. It was first necessary to determine the position of the annual ring borders from the local slope change of the grey level due to density variation. Next, each annual ring was divided into three parts, with 45% of its width allocated to earlywood and transition wood (TW, between earlywood and latewood) and 10% to latewood (Figure 4). These proportions were kept constant during imbibition.

The dimensional modifications of the ROI due to swelling affect the surface density and must be considered to compute the MC variations (Equations (6) and (8)). In the longitudinal direction, the images have no anatomical markers to follow possible variation. Fortunately, the hygro-expansion of wood is negligible in this direction (Perré 2007; Skaar 1988). In radial and tangential directions, the borders of the sample and of the growth rings were automatically detected from the local slope change of grey level to account for dimensional changes.

2.4 Theoretical MC at full saturation

The absolute variations in MC within the annual ring must be analyzed with caution. Indeed, due to their specific density, earlywood and latewood have different water storage capacities. Thus, the calculation of the saturation rate—as the ratio of MC over the theoretical MC at full saturation—is relevant to highlight the substantial heterogeneity of kinetics between earlywood and latewood.

The theoretical MC at full saturation X_{sat} is reached when both cell walls and lumens are saturated with water. It was estimated according to Equation (9) (Perré and Turner 2001) by assuming that (i) the sample porosity was fully saturated with liquid, and (ii) the volume of the pores remains constant in spite of shrinkage/swelling (Mariaux 1989).
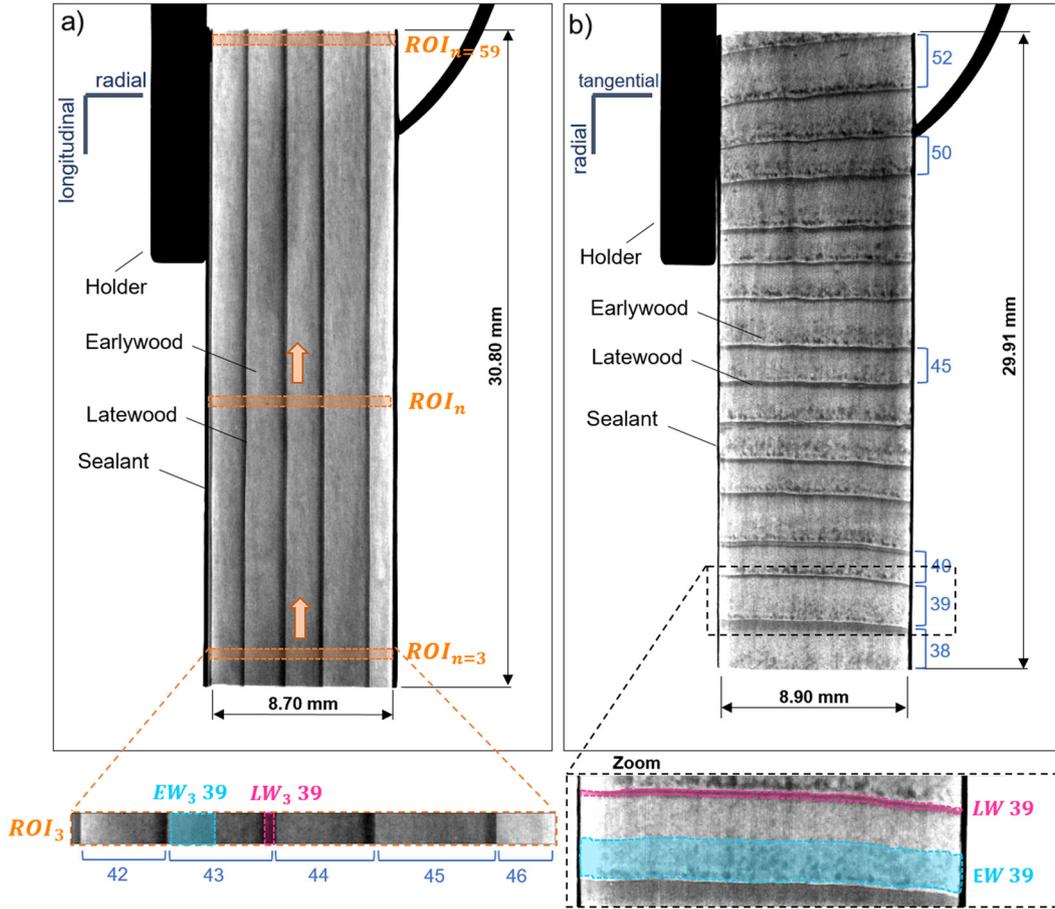
Figure 4: Principle of selected regions of interest (ROI) for imbibition experiment in longitudinal (a) and radial directions (b).

Table 2: Values of the coefficients L_0, L_1, λ and α.

L_0	L_1	λ	A
−0.04713	−0.65172	2.54123	0.71229

$$X_{sat} = \left(\rho_0 \cdot X_{fsp} + \left(1 - \frac{\rho_0}{\rho_{wall}} \right) \cdot \rho_l \right) / \rho_0 \qquad (9)$$

with ρ_l the liquid water density at 20 °C (1000 kg/m^3) and ρ_{wall} the density of the cell wall (1530 kg/m^3) (Siau 1984).

This calculation was applied to the whole sample or to each ROI. In the latter case, according to Equation (9), local anhydrous density was required to estimate the theoretical MC at full saturation. The surface density ρ_{eq}^* of the considered ROI was identified from the non-linear relation (Equation (5)) using the uncoated sample and assuming a uniform initial MC. Next, the local anhydrous surface density ρ_0^* was determined from Equation (6). For this calculation, it was assumed (i) that the cell wall composition was the same in earlywood and latewood, and (ii) the contributions of extractives and resin to X-ray attenuation were uniform. To obtain the local anhydrous density ρ_0 (kg/m^3), the local anhydrous surface density ρ_0^* had to be divided by the sample thickness $d_{correct}$ crossed by the X-ray beam, after having

taken into account the swelling from the anhydrous to the initial state to Equation (10):

$$d_{correct} = d \cdot \frac{1}{1 + \frac{R}{1-R} \cdot \frac{X}{X_{fsp}}} \qquad (10)$$

with d the initial sample thickness, R the total shrinkage according to the wood direction of the thickness (Perré and Huber 2007), and X_{fsp} the fiber saturated point. d and R were considered as constant regardless of location and X_{fsp} of spruce set at 29% (Siau 1984).

3 Results and discussion

3.1 Local moisture content at full saturation versus anhydrous density

The anhydrous density and the theoretical MC at full saturation are plotted in Figure 5 along the width of ROI #3 of the sample used for studying the longitudinal imbibition. The average anhydrous density determined for the entire sample was 412 kg/m^3. The anhydrous density within the rings varied from 250–280 kg/m^3 in

earlywood to 850–1100 kg/m^3 in latewood, depending on the ring. These values highlight the anatomical structure of spruce (softwood), with thinner cell walls and larger lumens in earlywood than in latewood (Butterfield and Meylan 1980). The results were in strong accordance with results from other studies using the micro-densitometry method or optical measurement (Decoux et al. 2004; Polge 1966). As expected, X_{sat} is minimal in latewood (50–70%) and maximal in earlywood (330–380%).

3.2 Longitudinal direction

3.2.1 General trends

Figure 6 shows the general trends from the corrected images for the selected times. Water uptake was observed through the variation of the grey level within the sample. A clear moisture uptake was already visible after 50 s, indicating a swift water uptake process at the early stages (Figure 6a). After 96 h, the moisture migration reached approximately half the height of the sample (Figure 6a–d). The front imbibition during the test shows a non-homogeneous migration among and within annual rings (Figure 6a–d). In the ring located on the right side (#46), the grey level change due to water uptake was less pronounced than the one next to it, signifying a lower moisture content. From this observation, no significant moisture transfers in the radial direction seemed to have taken place through ring border #45–46. These results were in accordance with previous work showing heterogeneous water uptake in space and time between and within these rings
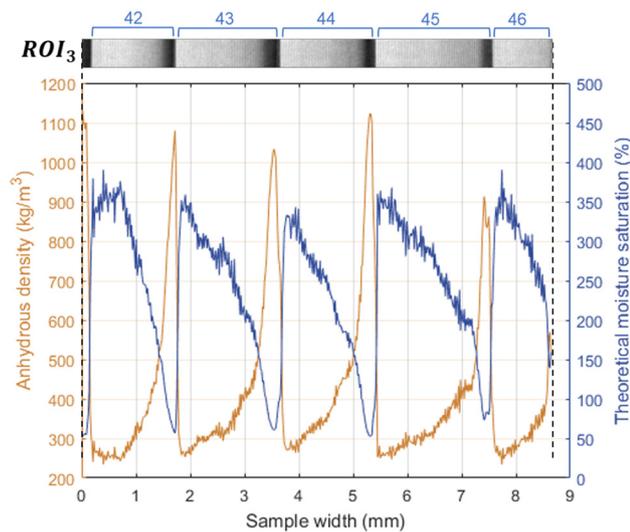
(Derome et al. 2005; Desmarais et al. 2016; Sandberg and Salin 2012).

3.2.2 Quantitative analysis

Moisture content determination along the length of the sample was carried out for each ROI. During imbibition, the bottom of the sample was not available because of liquid water. For this reason, the measurement started from the ROI #3—that is, at a distance of 1.31 mm above the level of the liquid. The average moisture content in the sample was thus estimated by assuming ROIs #1 and #2 to have the same moisture content as ROI #3. The variations of the mean MC and the MC of nine ROIs are plotted versus the square root of time in Figure 7. These ROIs were selected to capture the kinetics of moisture uptake both at short intervals close to the wet surface and at long intervals throughout its height.
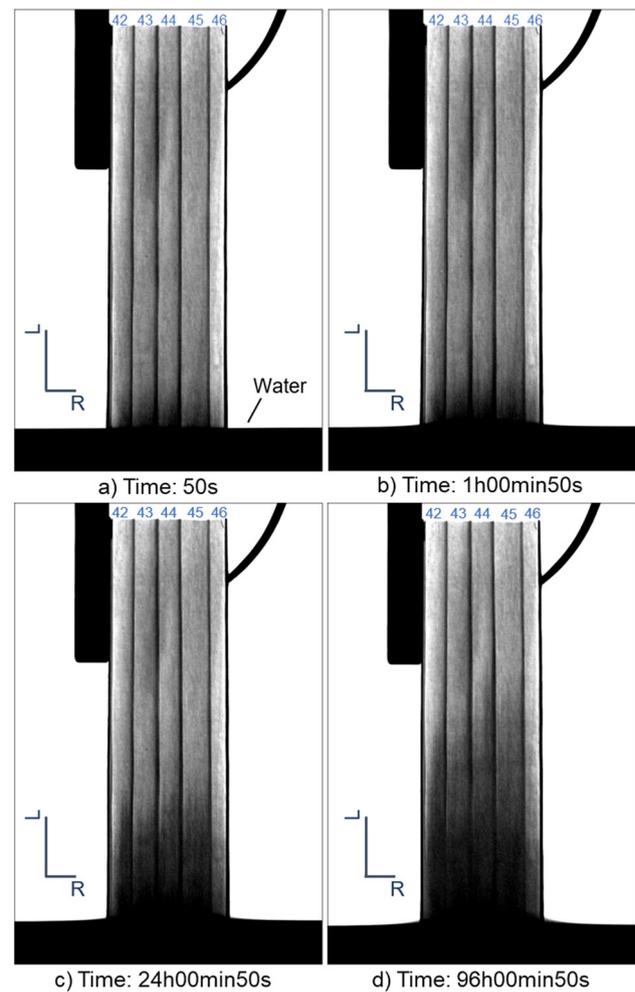

Figure 5: Distribution of anhydrous densities along the width of the sample for ROI #3.

Figure 6: Water uptake in Norway spruce along longitudinal direction at several different times.
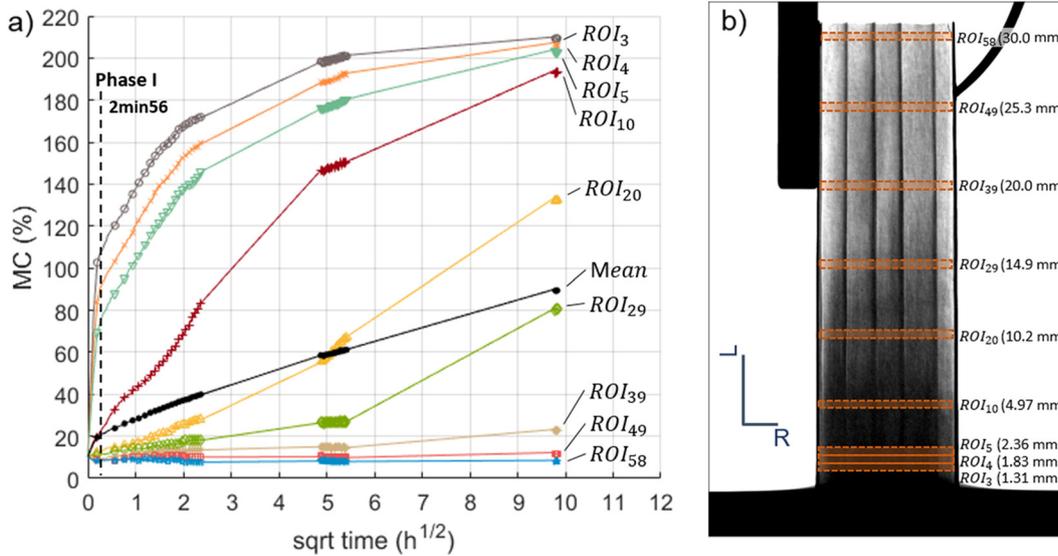
Figure 7: (a) Moisture content kinetic for the selected ROI in longitudinal direction. (b) Location of the ROI in the sample.

The moisture uptake of the ROIs located closed to the contact surface involved three phases and did not follow a linear slope. A rapid moisture uptake was observed at brief intervals (2 min 56 s) over a short distance (up to ROI #5). As the length concerned by this rapid rise was about 2 mm, this could be explained by the invasion of the open tracheids lumens in contact with the liquid. However, this rapid increase was far from full saturation; obviously, just one fraction of tracheids were affected by this brief phase. The second phase—which involved the connections between the tracheids (the bordered pits) and the diffusion of bound water through the cell walls—was much slower. Furthermore, a constant increase of MC was observed as the square root of time due to migration into the connected porosity until it reached the last phase, where almost all of the lumens became filled.

The general trend for all positions above one tracheid length (ROI #10 to #29) depicted a similar behavior but shifted in duration as the ROI position got away from the contact surface. This trend consisted of a slow progressive initial increase of MC, followed by a more rapid increase when the imbibition front reached the considered location. At the end of the imbibition, the distribution of MC measured over the height of the sample exhibit a strong heterogeneity. No significant change in MC was observed at the top of the sample (ROI #58), whereas it increased from 10.1% toward the asymptotic value of ca. 210% at the bottom (ROI #3). As a result, the mean MC of the sample changed rapidly at the early stages and kept increasing, following a linear slope, until the end of the test due to the wetting front continued progression in the highest part of

the sample. The mean MC measured was very close to the MC values obtained by the gravimetric method, at 89.1 and 92.1%, respectively. These values were consistent considering the respective accuracies of both methods.

Moisture absorption kinetics in earlywood (EW) and latewood (LW) were presented for ROI #3 and #20, respectively, located at 1.31 and 10.18 mm from the contact surface. The two locations were chosen to be as close as possible to the contact surface (#3) and above several successive tracheids (#20). To highlight the strong heterogeneity of kinetics between earlywood and latewood, the results for the ROIs are presented in MC (Figure 8a.1—ROI #3 and Figure 8a.2—ROI #20) and saturation (Figure 8b.1—ROI #3 and Figure 8b.2—ROI #20). In ROI #3, moisture absorption kinetics mainly involves three phases for earlywood and two phases for latewood. The first phase (until 2 min, 56 s) was characterized by a rapid increase in the moisture content for both earlywood and latewood, confirming a direct rise in open tracheids. At the end of this phase, the rate of water absorption decreased sharply in latewood. In comparison, the moisture uptake rate in earlywood changed but was still increasing rapidly. The third phase in earlywood was characterized by a slowing down of moisture absorption kinetic as the moisture approached full saturation.

The results for the ROI #20 located at 10.18 mm from the contact surface (Figure 8b.2) confirmed a significant increase of MC in latewood before earlywood, as qualitatively reported by neutron imaging (Desmarais et al. 2016). After 2 h of imbibition, a significant change of moisture content was visible in latewood for three rings, whereas it
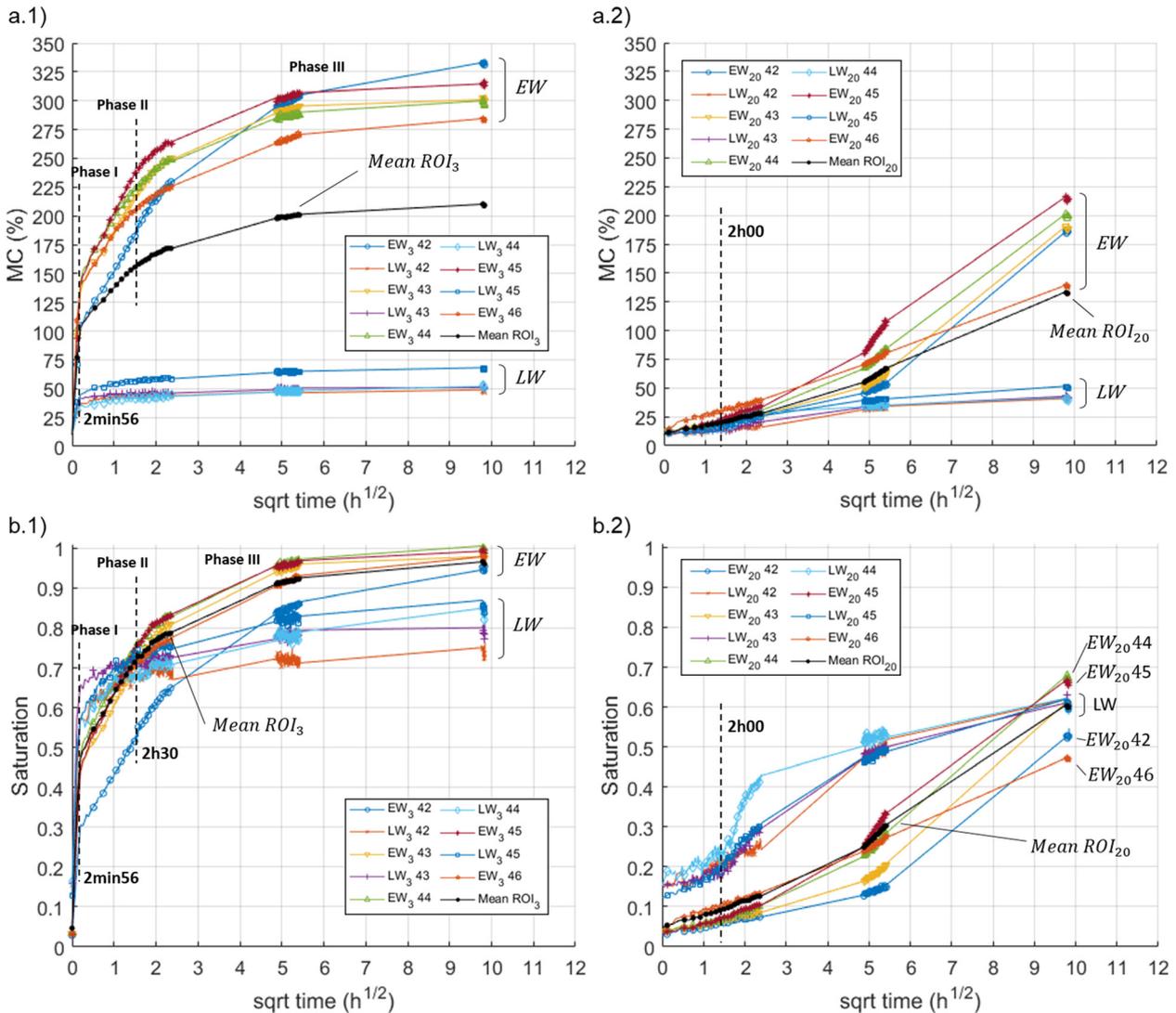
Figure 8: Moisture absorption kinetics in EW and LW in MC (a) and saturation (b) for the ROI #3 (1) and #20 (2), respectively located 1.31 and 10.18 mm from the contact surface.

began after 24 h in earlywood. To explain these differences, one must keep in mind that the average density of the ROIs located in latewood was approximately three times larger than those in earlywood, 970 versus 283 kg/m³. This density variation along the annual ring is due to the thicker cell wall, and smaller lumen size in latewood compare with earlywood (Kollmann and Côté 1968). This anatomical structure induces a large number of aspirated pits in earlywood compared with latewood (Siau 1984). Indeed, the size of the small pits in latewood results in a more rigid membrane than in earlywood due to the smaller lumen size.

For this reason, they are less prone to be aspirated when liquid water is removed from the fresh board. Consequently, liquid migration is facilitated in latewood,

as reported in Almeida et al. (2008), using MRI. In earlywood, most pits are aspirated, leading to a more complex liquid migration into the pore network. In the early stages of this experiment, only a part of the directly accessible tracheids was involved in fluid migration. Then, water migrated from one cell to the others, explaining the second phase of moisture uptake. The sudden decrease of MC change rate in latewood of ROI #3 at around 65% of saturation rate, followed by a slight increase, could be explained by the fact that free water represented approximately 50% of moisture content at full saturation, while it was 90% for earlywood. Indeed, in latewood, almost all of the lumens of tracheids could be filled quickly. The slow and residual moisture increase until the end of the experiment might be explained by water migration in less

connected tracheids or in ray cells. These results highlighted the complex moisture migration in the pore network that were partially connected, leading to heterogeneity of water migration in space and time.

3.3 Radial direction

3.3.1 General trends

For the imbibition test in radial direction, the face of the sample in contact with liquid water was located in the earlywood of ring #38. In Figure 9a, the corrected images reveal the qualitative evolution of moisture uptake over time. The swelling of the sample along its tangential direction was clearly visible from 50 s of contact with the liquid. Next, the swelleing extented slightly until the latewood part of this ring, but no further swelling was observed at higher sample locations until the end of imbibition. The water reached the latewood zone in the first annual ring but did not seem to migrate further into the sample. Latewood located in this first annual ring acted as a barrier to water migration, as suggested by Meder et al. (2003), even though this was not observed by Sedighi-Gilani et al. (2012). To investigate whether this behavior was due to a distinct feature of Ring #38, a second experiment with the same sample and the same initial MC was performed after removing Ring #38. In this case, the face in contact with the liquid was located in the earlywood of Ring #39 (Figure 9b). The results showed a rapid moisture uptake at the early stages, with swelling beyond the first ring. Then, the liquid uptake and swelling observed in latewood from #39 to #41 indicated that the liquid was able to cross the annual ring border and migrate in several upper annual rings. To explain such different behaviors, enlargements of the bottom of the sample before and after each experiment is depicted in Figure 10. The relatively large latewood thickness of Ring #38—which is unusual for normal spruce wood—suggested the presence of compressive wood (Figure 10a.1). At the end of the first experiment, a horizontal line was visible in the transient zone between earlywood and latewood in Ring #38 (Figure 10a.2). The moisture migration seemed to be blocked at this level, signaling a discontinuity in the connected porosities. During the second experiment—where no compression wood was present—liquid water was visible inside the lumens of several annual rings (dark spots). The image in Figure 10b.2 shows that series of lumens were filled preferentially in the vertical direction—that is, in the radial direction—with spatial heterogeneity of filled lumens. From these results, it can be concluded that compression wood is a barrier to radial transfer. In normal wood, the liquid was able to cross the annual ring border. As for longitudinal transfer, this occurred through connected tracheids first and then spread over the remaining cells, from one to the others.

3.3.2 Quantitative analysis

The kinetics of the MC for the selected ROIs versus the square root of time are depicted in Figure 11. In both tests, a rapid increase in MC was observed at the early stages close to the contact surface and below the first ring boundary. However, in the ring located right above the first annual ring, no significant moisture uptake was visible in the first experiment (Figure 11a—EW 39), whereas MC saturation rate reached almost 40% in ring #40 in the second experiment. The MC in the upper ring, #41, also started to increase after 30 min of imbibition. To further understand these different behaviors, the annual ring in contact with the liquid was investigated in both experiments. The closest area accessible above the water was located in the transition wood TW 38 in the first experiment and TW 39 in the second (Figure 11). The saturation rate of both ROIs reached 55% in less than 3 min. However, in latewood, the saturation rate was lower in Ring #38 than in Ring #39. To highlight the particular behavior of Ring #38 in the first experiment, the ROI LW 38 was divided into two equal parts within the ring along the radial direction, called LW-1 38 and LW-2 38 (Figure 11a.2). Both ROIs showed a change in moisture uptake kinetics. The one located below (closest to the contact surface, i.e., LW-1 38) reached a saturation rate near 70%, whereas the second one (LW-2 38) remained close to 40%. From these results, it can be deduced that the moisture migration ceased before the first annual ring border.

The relatively large latewood zone in this location suggests the presence of compression wood. To further investigate and confirm the observation made from the qualitative and quantitative analysis, images of a twin sample (located nearby in the same longitudinal direction) were obtained using an Environmental Scanning Electron Microscope (ESEM) in "Low Vac" mode (Figure 12). In softwoods, due to the high value of microfibril angle, compression wood has thick cell walls and round cells, which forms intercellular spaces at the intersection of three cells (Butterfield and Meylan 1980). Given that compression wood is formed as a reaction to environmental stress,
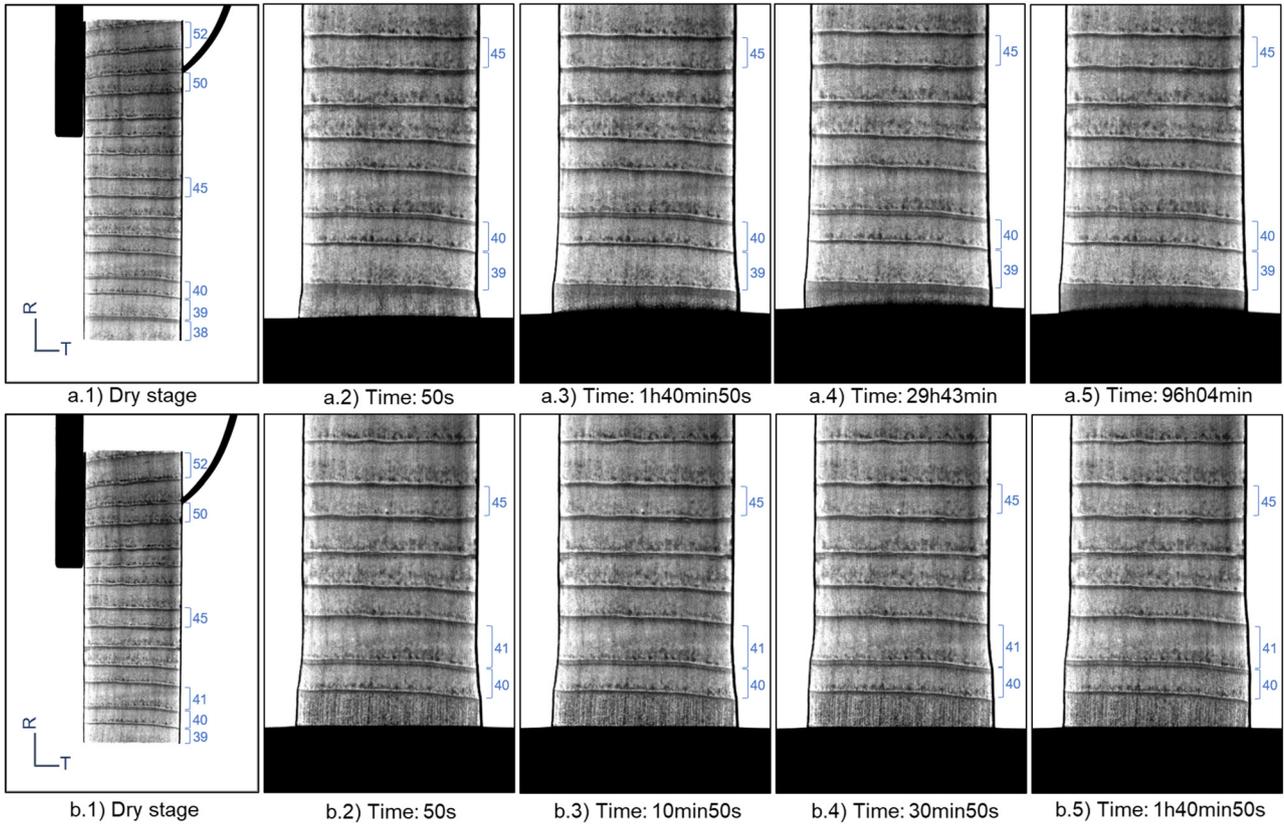
Figure 9: Water uptake in Norway spruce along the radial direction at several different times: (a) in the first test (including Ring #38) and (b) in the second test (after removing the Ring #38).
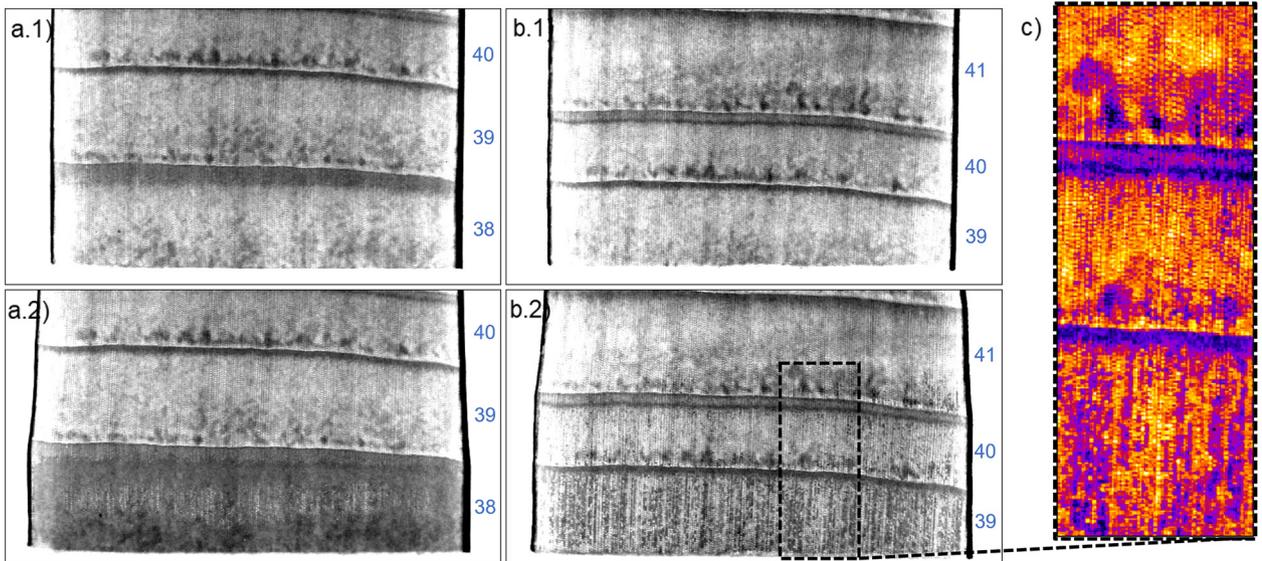

Figure 10: Bottom of the sample before (subscript 1) and at the end (subscript 2) of the first imbibition experiment (a) and second and (b). c) Zoom on the area pointed out by the dashed line, with the LUT "Fire".
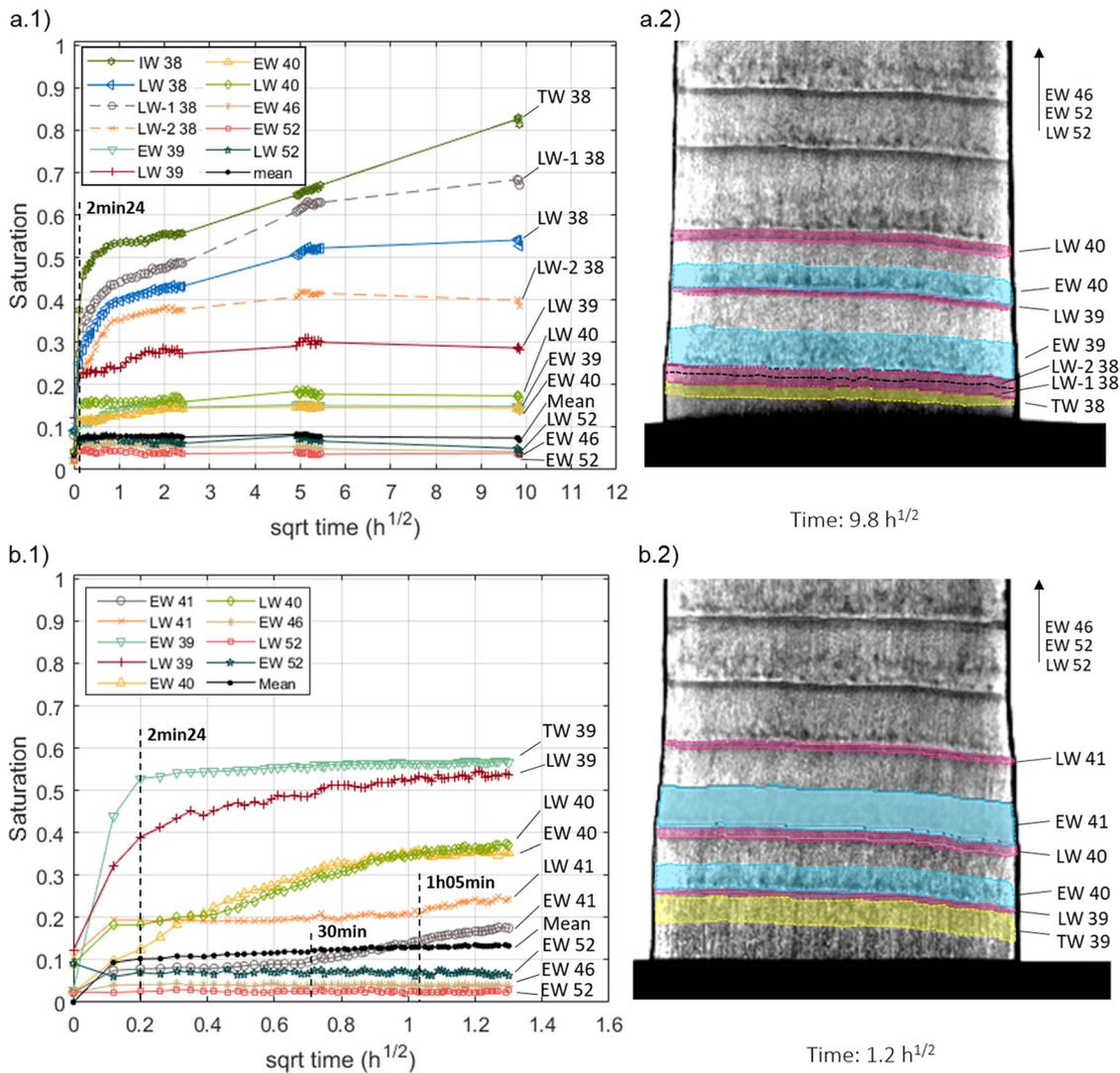
Figure 11: Moisture content kinetic for the selected ROI in the radial direction: (a) in the first test (including Ring #38) and (b) in the second test after removing Ring #38.

the tree responds proportionally by forming thicker cell walls (Donaldson and Singh 2013; Gardiner et al. 2014). The current ring corresponds to mild compression wood because the thick cell wall with a partially circular shape and no bordered pits were observed (Warensjö 2003). These particular features—not present in normal wood—lead to a lower bound water diffusivity compared with the one measured in normal wood (Siau 1984; Tarmian et al. 2012). In addition, compression wood is less permeable due to the smaller number of pits, which do not allow liquid to migrate easily from one cell to the others (Mayr et al. 2006; Tarmian and Perré 2009). These chemical and physical modifications compared with the properties of normal wood easily explain why compression wood acts as a barrier to moisture migration in the radial direction.

4 Conclusion and perspectives

In this study, X-ray imaging was used as a non-destructive technique to investigate the temporal evolution and spatial distribution of moisture in Norway spruce during imbibition in longitudinal and radial directions. The original work provides an accurate description of moisture absorption kinetics and emphasises the difference between the behaviors of earlywood and latewood. The main results of these experiments can be summarized as follows:

- In the longitudinal direction:
    - The migration of liquid was faster in the latewood than in the earlywood due to non-aspirated pits facilitating the migration of the liquid.
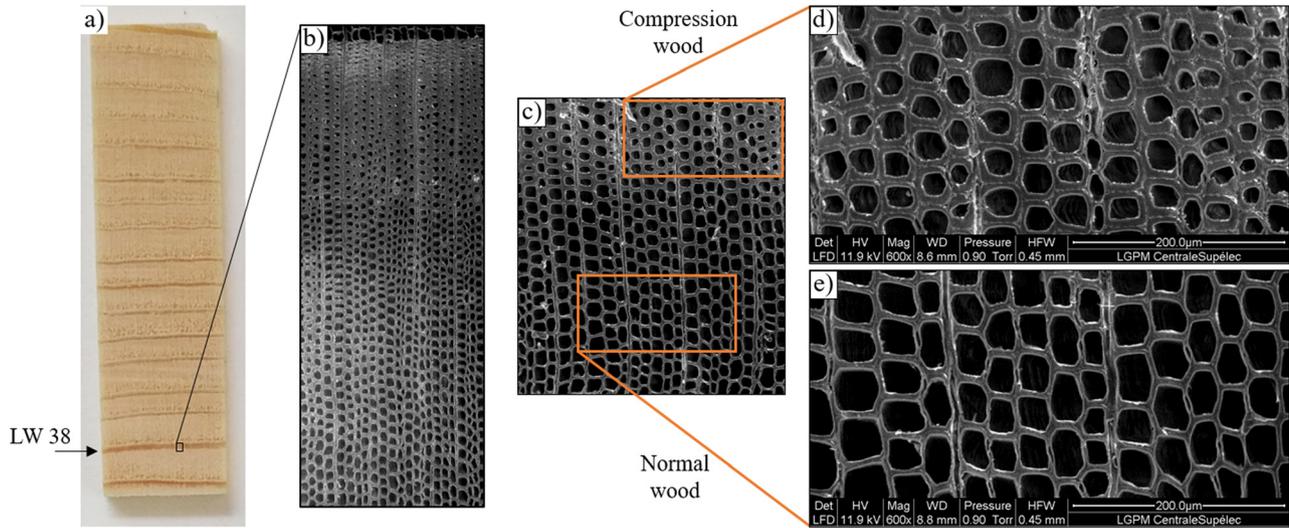
Figure 12: ESEM images of the annual ring of interest 38 from twin sample (photography) used for imbibition experiment in radial direction.

– The liquid migration was more complex in early-wood, with two-time constants: the shortest for liquid migration in the few connected lumens and the second and a longer one to progressively reach full saturation by migration from one cell to another in the radial direction.
– In the radial direction:
– Compression wood acted as a barrier to moisture migration due to its anatomical characteristics, with few pits in large cell walls and high amounts of lignin.
– In normal wood, as for longitudinal migration, the liquid was able to flow in the few continuous tracheid pathways with unaspirated pits, explaining the punctual patterns, followed by a slow propagation of the filled zones.

The present experimental data from 2D X-rays imaging can be helpful to improve numerical model prediction simulating coupled heat and mass transfer in timber construction and, in general, in porous building materials. The relevance of using a homogeneous or heterogeneous model could be investigated with the possibility of determining relative liquid permeability in latewood and earlywood using the inverse method. By analyzing the impact of wood density on relative liquid permeability, the discrepancy reduction between measurements and simulations of transfers may be reduced, thus improving performance and durability of wooden construction.

Appendix: Choice of the sealant adapted to X-ray imaging and wood

Preliminary tests without any sealant were performed using X-ray imaging but were not analyzed because of the capillary migration of water at the surface of the sample. Consequently, the moisture content and speed velocity would have been overestimated (De Meijer and Militz 2001). This effect is visible in Figure 5 of Desmarais et al. (2016), where imbibition experiments in the wood radial direction were performed. When the lateral surfaces were not covered with an impermeable and hydrophobic coating, liquid water went up on the longitudinal/tangential plane and thus entered the material via the lumens of tracheids connected by pits or reached the top of the sample. This disturbed moisture migration assessment and monitoring of the imbibition phenomenon. In this study, several coated products were tested, including the following sealants:

- epoxy resin (Loctite EA3430) combined with aluminum foil → epoxy resin breaks due to swelling;
- waterproof paint (AquaStop v33) → no liquid water repellent and penetrates the lumens;
- bituminous spray (SINTO) → too fragile;
- wood stain (Mauler) → penetrates into the lumen of tracheids;

- waterproof underlay under tile (ParexLanko) → high X-ray attenuation leading to loss of details. Presence of solid particles made it challenging to apply homogeneously to the wood surface;
- waterproof liquid rubber paint (Rubson, Liquid Rubber Plus) → do not penetrate the lumens, easy to apply using a brush, moderate X-ray attenuation, able to follow the dimensional variations, and waterproof.

Varnish was not studied because of its non-elasticity and its penetration in lumens.

Therefore, waterproof rubber paint (Rubson) was the best compromise for wood material and X-ray imaging. Figure 13 confirms the non-penetration of the sealant into the material. The slices selected from a CT-3D scan performed at the dry stage (voxel size 7 μm) highlighted the local irregularity of the sample surface. The black stains, mainly located in earlywood, were due to the sealant.

References

Almeida, G., Gagné, S., and Hernández, R.E. (2007). A NMR study of water distribution in hardwoods at several equilibrium moisture contents. Wood Sci. Technol. 41: 293–307.

Almeida, G., Leclerc, S., and Perre, P. (2008). NMR imaging of fluid pathways during drainage of softwood in a pressure membrane chamber. Int. J. Multiphas. Flow 34: 312–321.

Baettig, R., Rémond, R., and Perré, P. (2006). Measuring moisture content profiles in a board during drying: a polychromatic X-ray
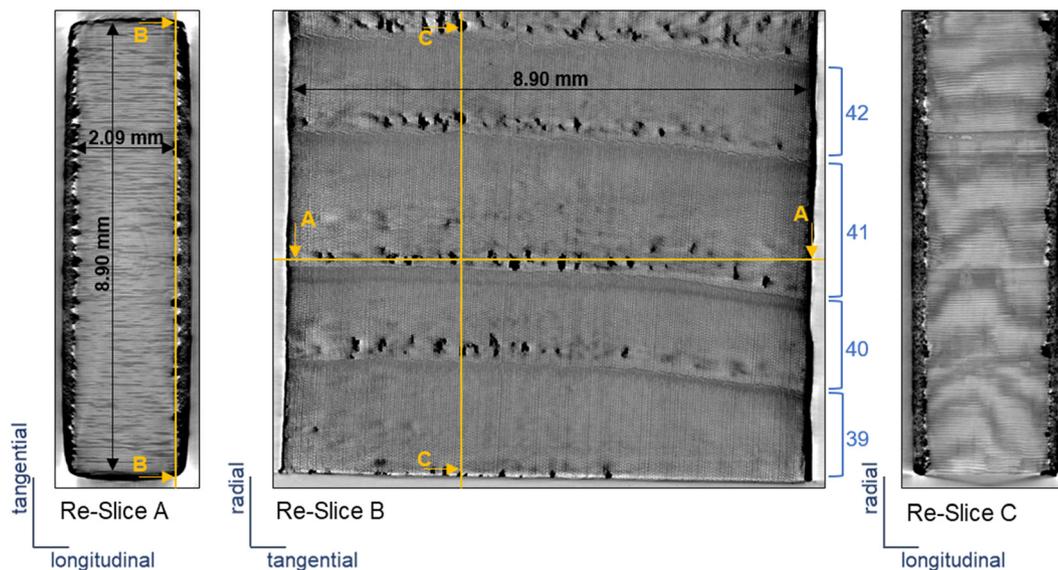
Figure 13: Selected slices from a CT-3D scan of Sample B.

system interfaced with a vacuum/pressure laboratory kiln. Wood Sci. Technol. 40: 261–274.

Bouali, A., Rémond, R., Almeida, G. and Perré, P. (2012) Thermo-diffusion in wood: X-ray MC profiles analysed using a 2-D computational model. In *Proceedings of the 18th international drying symposium, China, Xiamen*.

Butterfield, B.G. and Meylan, B.A. (Eds.) (1980). *Three-dimensional structure of wood*. Dordrecht: Springer Netherlands.

Cullity, B.D. (1956). *Elements of X-ray diffraction*. Addison-Wesley Publishing.

Decoux, V., Varcin, E., and Leban, J.-M. (2004). Relationships between the intra-ring wood density assessed by X-ray densitometry and optical anatomical measurements in conifers. Consequences for the cell wall apparent density determination. Ann. For. Sci. 61: 251–262.

De Meijer, M. and Militz, H. (2000). Moisture transport in coated wood. Part 1: analysis of sorption rates and moisture content profiles in spruce during liquid water uptake. Holz als Roh- Werkst. 58: 354–362.

De Meijer, M. and Militz, H. (2001). Moisture transport in coated wood. Part 2: influence of coating type, film thickness, wood species, temperature and moisture gradient on kinetics of sorption and dimensional change. Holz als Roh- Werkst. 58: 467–475.

Derome, D., Roels, S., and Carmeliet, J. (2005). Qualitative work to study water movement in wood, [Online]. In: Proceedings of the 7th symposium on building physics in the Nordic countries. Reykjavik, pp. 173–180.

Desmarais, G., Gilani, M.S., Vontobel, P., Carmeliet, J., and Derome, D. (2016). Transport of polar and nonpolar liquids in softwood imaged by neutron radiography. Transp. Porous Media 113: 383–404.

Donaldson, L.A. and Singh, A.P. (2013). Formation and structure of compression wood. In: Fromm, J. (Ed.). *Cellular aspects of wood formation. Plant cell monographs*. Berlin/Heidelberg: Springer, pp. 225–256, [Online].

Gardiner, B., Barnett, J., Saranpää, P., and Gril, J. (2014). *The biology of reaction wood. Springer series in wood science*. Berlin/Heidelberg: Springer.

Gezici-Koç, Ö., Erich, S.J.F., Huinink, H.P., van der Ven, L.G.J., and Adan, O.C.G. (2017). Bound and free water distribution in wood during water uptake and drying as measured by 1D magnetic resonance imaging. Cellulose 24: 535–553.

Guinier, A. (1964). *Theory and technics for X-ray crystallography*. Paris: Dunod.

Hameury, S. and Sterley, M. (2006). Magnetic resonance imaging of moisture distribution in *Pinus sylvestris* L. exposed to daily indoor relative humidity fluctuations. Wood Mater. Sci. Eng. 1: 116–126.

van Houts, J.H., Wang, S., Shi, H., Pan, H., and Kabalka, G.W. (2004). Moisture movement and thickness swelling in oriented strandboard, part 1. Analysis using nuclear magnetic resonance microimaging. Wood Sci. Technol. 38: 617–628.

Johansson, J. and Kifetew, G. (2010). CT-scanning and modelling of the capillary water uptake in aspen, oak and pine. Eur. J. Wood Wood Prod. 68: 77–85.

Johansson, P., Bok, G., and Ekstrand-Tobin, A. (2013). The effect of cyclic moisture and temperature on mould growth on wood compared to steady state conditions. Build. Environ. 65: 178–184.

Kollmann, F.F.P., and Côté, W.A. (1968). *Principles of wood science and technology. I: solid wood*, Vol. 1. Springer-Verlag.

Krabbenhoft, K. and Damkilde, L. (2004). Double porosity models for the description of water infiltration in wood. Wood Sci. Technol. 38: 641–659.

Lepage, R. (2012). *Moisture response of wall assemblies of cross-laminated timber construction in cold Canadian climates*. University of Waterloo, [Online].

Mariaux, A. (1989). La section transversale de fibre observée avant et après séchage sur bois massif. Bois Forets Tropiques 221: 65–76.

Mayr, S., Bardage, S., and Brandstrom, J. (2006). Hydraulic and anatomical properties of light bands in Norway spruce compression wood. Tree Physiol. 26: 17–23.

McMillen, J.M. (1958). *Stresses in wood during drying*. US Forest Service Report FPL.

Meder, R., Codd, S.L., Franich, R.A., Callaghan, P.T., and Pope, J.M. (2003). Observation of anisotropic water movement in *Pinus radiata* D. Don sapwood above fiber saturation using magnetic resonance micro-imaging. Holz als Roh- Werkst. 61: 251–256.

NF EN 13183-1 (2002). *Moisture content of a piece of sawn timber – part 1: determination by oven dry method*.

NF EN 13183-2 (2002). *Moisture content of a piece of sawn timber – part 2: estimation by electrical resistance method*.

Niemz, P. and Mannes, D. (2012). Non-destructive testing of wood and wood-based materials. J. Cult. Herit. 13: S26–S34.

Passarini, L., Malveau, C., and Hernández, R.E. (2015). Distribution of the equilibrium moisture content in four hardwoods below fiber saturation point with magnetic resonance microimaging. Wood Sci. Technol. 49: 1251–1268.

Pease, B.J., Scheffler, G.A., and Janssen, H. (2012). Monitoring moisture movements in building materials using X-ray attenuation: influence of beam-hardening of polychromatic X-ray photon beams. Construct. Build. Mater. 36: 419–429.

Perré, P. (2007). Experimental device for the accurate determination of wood-water relations on micro-samples. Holzforschung 61: 419–429.

Perré, P. (2011). A review of modern computational and experimental tools relevant to the field of drying. Dry. Technol. 29: 1529–1541.

Perré, P. and Huber, F. (2007). Measurement of free shrinkage at the tissue level using an optical microscope with an immersion objective: results obtained for Douglas fir (*Pseudotsuga menziesii*) and spruce (*Picea abies*). Ann. For. Sci. 64: 255–265.

Perré, P., and Thiercelin, F. (2004). Evidence of dual scale porous mechanisms during fluid migration in hardwood species: part I: using the attenuation of a polychromatic X-ray beam to determine the evolution of moisture content during imbibition of beech. Chin. J. Chem. Eng. 12: 773–782.

Perré, P., and Turner, I. (2001). Determination of the material property variations across the growth ring of softwood for use in a heterogeneous drying model. Part 1. Capillary pressure, tracheid model and absolute permeability. Holzforschung 55: 318–323.

Phillipson, M.C., Baker, P.H., Davies, M., Ye, Z., McNaughtan, A., Galbraith, G.H., and McLean, R.C. (2007). Moisture measurement in building materials: an overview of current methods and new approaches. Build. Serv. Eng. Technol. 28: 303–316.

Polge, H. (1966). Établissement des courbes de variation de la densité du bois par exploration densitométrique de radiographies déchantillons prélevés à la tarière sur des arbres vivants : applications dans les domaines Technologique et Physiologique. Ann. Des. Sci. For. 23: 1–206.

Ramage, M.H., Burridge, H., Busse-Wicher, M., Fereday, G., Reynolds, T., Shah, D.U., Wu, G., Yu, L., Fleming, P., Densley-Tingley, D., et al (2017). The wood from the trees: the use of timber in construction. Renew. Sustain. Energy Rev. 68: 333–359.

Roels, S. and Carmeliet, J. (2006). Analysis of moisture flow in porous materials using microfocus X-ray radiography. Int. J. Heat Mass Tran. 49: 4762–4772.

Sandberg, K. and Salin, J.-G. (2012). Liquid water absorption in dried Norway spruce timber measured with CT scanning and viewed as a percolation process. Wood Sci. Technol. 46: 207–219.

Schmidt, E.L., Riggio, M., Barbosa, A.R., and Mugabo, I. (2019). Environmental response of a CLT floor panel: lessons for moisture management and monitoring of mass timber buildings. Build. Environ. 148: 609–622.

Sedighi-Gilani, M., Griffa, M., Mannes, D., Lehmann, E., Carmeliet, J., and Derome, D. (2012). Visualization and quantification of liquid water transport in softwood by means of neutron radiography. Int. J. Heat Mass Tran. 55: 6211–6221.

Seltzer, S. (1987). *XCOM-photon cross sections database, NIST standard reference database 8*.

Siau, J.F. (1984). *Transport process in wood*. Berlin: Springer.

Skaar, C. (1988). *Wood-water relations. Springer series in wood science*. Berlin/Heidelberg: Springer.

Tarmian, A., and Perré, P. (2009). Air permeability in longitudinal and radial directions of compression wood of *Picea abies* L. and tension wood of *Fagus sylvatica* L. Holzforschung 63: 352–356.

Tarmian, A., Remond, R., Dashti, H., and Perré, P. (2012). Moisture diffusion coefficient of reaction woods: compression wood of *Picea abies* L. and tension wood of *Fagus sylvatica* L. Wood Sci. Technol. 46: 405–417.

Tiemann, H.D. (1919). An analysis of the internal stresses which occur in wood during the progress of drying from the green condition, with a brief discussion of the physical properties which affect these stresses. J. Franklin Inst. 188: 27–50.

Tietze, A., Ott, S., Boulet, S., Gradeci, K., Labonnote, N., Grynning, S., Noreen, J., and Anna, P. (2017). *Tall timber facades – identification of cost-effective and resilient envelopes for wood constructions*. Technical University Munich.

Tiitta, M. and Olkkonen, H. (2002). Electrical impedance spectroscopy device for measurement of moisture gradients in wood. Rev. Sci. Instrum. 73: 3093–3100.

Viitanen, H. (1994). Factors affecting the development of biodeterioration in wooden constructions. Mater. Struct. 27: 483–493.

Warensjö, M. (2003). Compression wood in Scots pine and Norway spruce: distribution in relation to external geometry and the impact on dimensional stability in sawn wood In: *Acta Universitatis Agriculturae Sueciae Silvestria*, Vol. 298. Umeå: Swedish University of Agricultural Sciences.

Zhou, M., Caré, S., Courtier-Murias, D., Faure, P., Rodts, S., and Coussot, P. (2018). Magnetic resonance imaging evidences of the impact of water sorption on hardwood capillary imbibition dynamics. Wood Sci. Technol. 52: 929–955.